

# Models of rapidly rotating neutron stars: remnants of accretion-induced collapse

Yuk Tung Liu<sup>★</sup> and Lee Lindblom<sup>★</sup>

*Theoretical Astrophysics, California Institute of Technology, Pasadena, CA 91125, USA*

Accepted 2001 February 1. Received 2001 January 30; in original form 2000 December 13

## ABSTRACT

Equilibrium models of differentially rotating nascent neutron stars are constructed, which represent the result of the accretion-induced collapse of rapidly rotating white dwarfs. The models are built in a two-step procedure: (1) a rapidly rotating pre-collapse white dwarf model is constructed; (2) a stationary axisymmetric neutron star having the same total mass and angular momentum distribution as the white dwarf is constructed. The resulting collapsed objects consist of a high-density central core of size roughly 20 km, surrounded by a massive accretion torus extending over 1000 km from the rotation axis. The ratio of the rotational kinetic energy to the gravitational potential energy of these neutron stars ranges from 0.13 to 0.26, suggesting that some of these objects may have a non-axisymmetric dynamical instability that could emit a significant amount of gravitational radiation.

**Key words:** instabilities – stars: interiors – stars: neutron – stars: rotation – white dwarfs.

## 1 INTRODUCTION

The accretion-induced collapse of a rapidly rotating white dwarf can result in the formation of a rapidly and differentially rotating compact object. It has been suggested that such rapidly rotating objects could emit a substantial amount of gravitational radiation (Thorne 1995), which might be observable by the gravitational wave observatories such as LIGO, VIRGO and GEO. It has been demonstrated that, if the collapse is axisymmetric, the energy emitted by gravitational waves is rather small (Müller & Hillebrandt 1981; Finn & Evans 1990; Mönchmeyer et al. 1991; Zwerger & Müller 1997). However, if the collapsed object rotates rapidly enough to develop a non-axisymmetric ‘bar’ instability, the total energy released by gravitational waves could be  $10^4$  times greater than in the axisymmetric case (Houser, Centrella & Smith 1994; Houser & Centrella 1996; Smith, Houser & Centrella 1996; Houser 1998).

Rotational instabilities of rotating stars arise from non-axisymmetric perturbations of the form  $e^{im\varphi}$ , where  $\varphi$  is the azimuthal angle. The  $m = 2$  mode is known as the *bar mode*, which is often the fastest-growing unstable mode. There are two kinds of instabilities. A *dynamical* instability is driven by hydrodynamics and gravity, and develops on a dynamical time-scale, i.e. the time for sound waves to travel across the star. A *secular* instability is driven by dissipative processes such as viscosity or gravitational radiation reaction, and the growth time is determined by the dissipative time-scale. These secular time-scales are usually much longer than the dynamical time-scale of the system. An interesting

class of secular and dynamical instabilities only occur in rapidly rotating stars. One convenient measure of the rotation of a star is the parameter  $\beta = T_{\text{rot}}/|W|$ , where  $T_{\text{rot}}$  is the rotational kinetic energy and  $W$  is the gravitational potential energy. Dynamical and secular instabilities set in when  $\beta$  exceeds the critical values  $\beta_d$  and  $\beta_s$  respectively. It is well known that  $\beta_d \approx 0.27$  and  $\beta_s \approx 0.14$  for uniformly rotating, constant-density and incompressible stars, the Maclaurin spheroids (Chandrasekhar 1969). Numerous numerical simulations in Newtonian theory show that  $\beta_d$  and  $\beta_s$  have roughly these same values for differentially rotating polytropes with the same specific angular momentum distribution as the Maclaurin spheroids (Tohline, Durisen & McCollough 1985; Durisen et al. 1986; Williams & Tohline 1988; Houser et al. 1994; Smith et al. 1996; Houser & Centrella 1996; Pickett, Durisen & Davis 1996; Houser 1998; New, Centrella & Tohline 1999). However, the critical values of  $\beta$  are smaller for polytropes with some other angular momentum distributions (Imamura & Toman 1995; Pickett et al. 1996; Centrella et al. 2000). Also general relativistic simulations suggest that the critical values of  $\beta$  are smaller than the classical Maclaurin spheroid values (Stergioulas & Friedman 1998; Shibata, Baumgarte & Shapiro 2000; Saijo et al. 2000).

Most of the stability analyses to date have been carried out on stars having simple ad hoc rotation laws. It is not clear whether these rotation laws are appropriate for the nascent neutron stars formed from the accretion-induced collapse of rotating white dwarfs.

New-born neutron stars resulting from the core collapse of massive stars with realistic rotation laws were studied by Mönchmeyer & Müller (1988), Janka & Mönchmeyer (1989a,b) and Zwerger & Müller (1997). The study of Mönchmeyer and

<sup>★</sup>E-mail: ytliu@its.caltech.edu (YTL); lindblom@tapir.caltech.edu (LL)

co-workers shows that the resulting neutron stars have  $\beta < 0.14$ . Zwerger & Müller carried out simulations of 78 models using simplified analytical equations of state (EOS). They found only one model having  $\beta > 0.27$  near core bounce. However,  $\beta$  remains larger than 0.27 for only about one millisecond, because the core re-expands after bounce and slows down. The pre-collapse core of that model is the most extreme one in their large sample: it is the most rapidly and most differentially rotating model, and it has the softest EOS. In addition, they found three models with  $0.14 < \beta < 0.27$ . Rapp, Müller & Ruffert (1998) subsequently performed 3D simulations of three of these models. They found that the model with  $\beta > 0.27$  shows a non-linear growth of a non-axisymmetric dynamical instability dominated by the bar mode ( $m = 2$ ). However, no instability is observed for the other two models during their simulated time interval of tens of milliseconds, suggesting that they are dynamically stable. Their analysis does not rule out the possibility that these models have non-axisymmetric secular instabilities, because the secular time-scale is expected to range from hundreds of milliseconds to a few minutes, much longer than their simulation time.

The aim of this paper is to improve Zwerger & Müller’s study by using realistic EOS for both the pre-collapse white dwarfs and the collapsed stars. For the pre-collapse white dwarfs, we use the EOS of a zero-temperature degenerate electron gas with electrostatic corrections. A hot, lepton-rich proto-neutron star is formed as a result of the collapse. This proto-neutron star cools down to a cold neutron star in about 20 s (see e.g. Burrows & Lattimer 1986), which is much longer than the dynamical time-scale. So we adopt two EOS for the collapsed stars: one is suitable for proto-neutron stars, and the other is one of the standard cold neutron star EOS.

Instead of performing the complicated hydrodynamic simulations, however, we adopt a much simpler method. We assume that (1) the collapsed stars are in rotational equilibrium with no meridional circulation, (2) any ejected material during the collapse carries a negligible amount of mass and angular momentum, and (3) the neutron stars have the same specific angular momentum distributions as those of the pre-collapse white dwarfs. The justifications of these assumptions will be discussed in Section 3. Our strategy is as follows. First we build the equilibrium pre-collapse rotating white dwarf models and calculate their specific angular momentum distributions. Then we construct the resulting collapsed stars having the same masses, total angular momenta and specific angular momentum distributions as those of the pre-collapse white dwarfs. All computations in this paper are purely Newtonian. In the real situation, if a dynamical instability occurs, the star will never achieve equilibrium. However, our study here can still give a useful clue to the instability issue.

The paper is organized as follows. In the next section we present equilibrium models of pre-collapse, rapidly and rigidly rotating white dwarfs. In Section 3, we construct the equilibrium models corresponding to the collapse of these white dwarfs. The stabilities of the collapsed objects are discussed in Section 4. Finally, we summarize our conclusions in Section 5.

## 2 PRE-COLLAPSE WHITE DWARF MODELS

### 2.1 Collapse mechanism

As mass is accreted on to a white dwarf, the matter in the white dwarf’s interior is compressed to higher densities. Compression releases gravitational energy and some of the energy goes into heat (Nomoto 1982). If the accretion rate is high enough, the rate of heat

generated by this *compressional heating* is greater than the cooling rate, and the central temperature of the accreting white dwarf increases with time.

The inner core of a carbon–oxygen (C–O) white dwarf becomes unstable when the central density or temperature becomes sufficiently high to ignite explosive carbon burning. Carbon deflagration releases nuclear energy and causes the pressure to increase. However, electron capture behind the carbon deflagration front reduces the temperature and pressure and triggers collapse. Such a white dwarf will either explode as a Type Ia supernova or collapse to a neutron star. Which path the white dwarf takes depends on the competition between the nuclear energy release and electron capture (Nomoto 1987). If the density at which carbon ignites is higher than a critical density of about  $9 \times 10^9 \text{ g cm}^{-3}$  (Timmes & Woosley 1992), electron capture takes over and the white dwarf will collapse to a neutron star. However, if the ignition density is lower than the critical density, carbon deflagration will lead to a total disruption of the whole star, leaving no remnant at all. More recent calculations by Bravo & García-Senz (1999), taking into account the Coulomb corrections to the EOS, suggest that this critical density is somewhat lower:  $6 \times 10^9 \text{ g cm}^{-3}$ . The density at which carbon ignites depends on the central temperature. The central temperature is determined by the balance between the compressional heating and the cooling and so strongly depends on the accretion rate and accretion time. For zero-temperature C–O white dwarfs, carbon ignites at a density of about  $10^{10} \text{ g cm}^{-3}$  (Salpeter & Van Horn 1969; Ogata, Iyetomi & Ichimaru 1991), which is higher than the above critical density. If the accreting white dwarf can somehow maintain a low central temperature during the whole accretion process, carbon will ignite at a density higher than the critical density, and the white dwarf will collapse to a neutron star. The fate of an accreting white dwarf as a function of the accretion rate and the white dwarf’s initial mass is summarized in two diagrams in the paper of Nomoto (1987) (see also Nomoto & Kondo 1991). Roughly speaking, low accretion rates ( $\dot{M} \lesssim 10^{-8} M_{\odot} \text{ yr}^{-1}$ ) and high initial mass of the white dwarf ( $M \gtrsim 1.1 M_{\odot}$ ), or very high accretion rates (near the Eddington limit) lead to collapse rather than explosion.

Under certain conditions, an accreting oxygen–neon–magnesium (O–Ne–Mg) white dwarf can also collapse to a neutron star (Nomoto 1987; Nomoto & Kondo 1991). The collapse is triggered by the electron captures of  $^{24}\text{Mg}$  and  $^{20}\text{Ne}$  at a density of  $4 \times 10^9 \text{ g cm}^{-3}$ . Electron captures not only soften the EOS and induce collapse, but also generate heat by  $\gamma$ -ray emission. When the star is collapsed to a central density of  $10^{10} \text{ g cm}^{-3}$ , oxygen ignites (Nomoto & Kondo 1991). At such a high density, however, electron captures occur at a faster rate than the oxygen burning, and the white dwarf collapses all the way to a neutron star.

In this section, we explore a range of possible pre-collapse white dwarf models. We assume that the white dwarfs are rigidly rotating. This is justified by the fact that the time-scale for a magnetic field to suppress any differential rotation,  $\tau_B$ , is short compared with the accretion time-scale. For example,  $\tau_B \sim 10^3 \text{ yr}$  if the massive white dwarf has a magnetic field  $B \sim 100 \text{ G}$ . We construct three white dwarf models using the EOS of a zero-temperature degenerate electron gas with Coulomb corrections derived by Salpeter (1961). All three white dwarfs are rigidly rotating at the maximum possible angular velocities. *Model I* represents a C–O white dwarf with a central density of  $\rho_c = 10^{10} \text{ g cm}^{-3}$ , the highest  $\rho_c$  that a C–O white dwarf can have before carbon ignition induces collapse. *Model II* is also a C–O white dwarf, but has a lower central density,

$\rho_c = 6 \times 10^9 \text{ g cm}^{-3}$ . This is the lowest central density for which a white dwarf can still collapse to a neutron star after carbon ignition. *Model III* is an O–Ne–Mg white dwarf with  $\rho_c = 4 \times 10^9 \text{ g cm}^{-3}$ , which is the density at which electron captures occur and induce the collapse. Since the densities are very high, the pressure is dominated by the ideal degenerate Fermi gas with electron fraction  $Z/A = 1/2$  that is suitable for both C–O and O–Ne–Mg white dwarfs. Coulomb corrections, which depend on the white dwarf composition through the atomic number  $Z$ , contribute only a few per cent to the EOS at high densities, so the three white dwarfs are basically described by the same EOS.

## 2.2 Numerical method

We treat the equilibrium rotating white dwarfs as rigidly rotating, axisymmetric, and having no internal motion other than the motion due to rotation. The Lichtenstein theorem (see Tassoul 1978) guarantees that a rigidly rotating star has reflection symmetry about the equatorial plane. We also neglect viscosity and assume Newtonian gravity. Under these assumptions the equilibrium configuration is described by the static Euler equation

$$\mathbf{v} \cdot \nabla \mathbf{v} = -\frac{\nabla P}{\rho} - \nabla \Phi, \quad (1)$$

where  $P$  is pressure,  $\rho$  is density and  $\Phi$  is the gravitational potential, which satisfies the Poisson equation

$$\nabla^2 \Phi = 4\pi G \rho, \quad (2)$$

where  $G$  is the gravitational constant. The fluid's velocity  $\mathbf{v}$  is related to the rotational angular frequency  $\Omega$  by  $\mathbf{v} = \Omega \boldsymbol{\omega} e_\phi$ , where  $\boldsymbol{\omega}$  is the distance from the rotation axis and  $e_\phi$  is the unit vector along the azimuthal direction. The EOS we use is barotropic, i.e.  $P = P(\rho)$ , so the Euler equation can be integrated to give

$$h = C - \Phi + \frac{\boldsymbol{\omega}^2}{2} \Omega^2, \quad (3)$$

where  $C$  is a constant. The enthalpy (per mass)  $h$  is given by

$$h = \int_0^P \frac{dP}{\rho}, \quad (4)$$

and is defined only inside the star. The boundary of the star is the surface with  $h = 0$ .

The equilibrium configuration is determined by Hachisu's self-consistent field method (Hachisu 1986): given an enthalpy distribution  $h_i$ , we calculate the density distribution  $\rho_i$  from the inverse of equation (4) and from the EOS. Next we calculate the gravitational potential  $\Phi_i$  everywhere by solving the Poisson equation (2). Then the enthalpy is updated by

$$h_{i+1} = C_{i+1} - \Phi_i + \frac{\boldsymbol{\omega}^2}{2} \Omega_{i+1}^2, \quad (5)$$

with  $C_{i+1}$  and  $\Omega_{i+1}^2$  determined by two boundary conditions. In Hachisu's (1986) paper, the axis ratio, i.e. the ratio of polar to equatorial radii, and the maximum density are fixed to determine  $C_{i+1}$  and  $\Omega_{i+1}^2$ . However, we find it more convenient in our case to fix the equatorial radius  $R_e$  and central enthalpy  $h_c$ , so that

$$C_{i+1} = h_c + \Phi_i(0), \quad (6)$$

$$\Omega_{i+1}^2 = -\frac{2}{R_e^2} [C_{i+1} - \Phi_i(A)], \quad (7)$$

where  $\Phi_i(0)$  and  $\Phi_i(A)$  are the gravitational potential at the centre and at the star's equatorial surface respectively. The procedure is repeated until the enthalpy and density distribution converge to the desired degree of accuracy.

We used a spherical grid with  $L$  radial spokes and  $N$  evenly spaced grid points along each radial spoke. The spokes are located at angles  $\theta_i$  in such a way that  $\cos \theta_i$  correspond to the zeros of the Legendre polynomial of order  $2L - 1$ :  $P_{2L-1}(\cos \theta_i) = 0$ . Because of the reflection symmetry, we only need to consider spokes lying in the first quadrant. Poisson's equation is solved using the technique described by Ipser & Lindblom (1990). The special choice of the angular positions of the radial spokes and the finite difference scheme make our numerical solution equivalent to an expansion in Legendre polynomials through order  $l = 2L - 2$  (Ipser & Lindblom 1990). Although the white dwarfs we consider here are rapidly rotating, the equilibrium configurations are close to spherical, as demonstrated in the next subsection. So a relatively small number of radial spokes are adequate to describe the stellar models accurately. We compared the results of  $(L, N) = (10, 3000)$  with  $(L, N) = (20, 5000)$  and find agreement to an accuracy of  $10^{-5}$ . The accuracy of the model can also be measured by the virial theorem, which states that  $2T_{\text{rot}} + W + 3\Pi = 0$  for any equilibrium star (see e.g. Tassoul 1978). Here  $T_{\text{rot}}$  is the rotational kinetic energy,  $W$  is the gravitational potential energy and  $\Pi = \int P d^3x$ . We define

$$\epsilon = \left| \frac{2T_{\text{rot}} + W + 3\Pi}{W} \right|. \quad (8)$$

All models constructed in this section have  $\epsilon \approx 10^{-7}$ .

## 2.3 Results

We constructed three models of rigidly rotating white dwarfs. All of them are maximally rotating: material at the star's equatorial surface rotates at the local orbital frequency. Models I and II are C–O white dwarfs with central densities  $\rho_c = 10^{10} \text{ g cm}^{-3}$  and  $\rho_c = 6 \times 10^9 \text{ g cm}^{-3}$  respectively; model III is an O–Ne–Mg white dwarf with  $\rho_c = 4 \times 10^9 \text{ g cm}^{-3}$ . The properties of these white dwarfs are summarized in Table 1. We see that the angular momentum  $J$  decreases as the central density  $\rho_c$  increases, because the white dwarf becomes smaller and more centrally condensed.

**Table 1.** The central density  $\rho_c$ , mass  $M$ , angular momentum  $J$ , rotational frequency  $\Omega$ , rotational kinetic energy  $T_{\text{rot}}$ , the ratio of rotational kinetic energy to gravitational energy  $\beta$ , equatorial radius  $R_e$  and polar radius  $R_p$  of three rigidly and maximally rotating white dwarfs.

	Composition	$\rho_c$ ( $\text{g cm}^{-3}$ )	$M$ ( $M_\odot$ )	$J$ ( $\text{g cm}^2 \text{ s}^{-1}$ )	$\Omega$ ( $\text{rad s}^{-1}$ )	$T_{\text{rot}}$ (erg)	$\beta$	$R_e$ (km)	$R_p$ (km)
Model I	C–O	$10^{10}$	1.47	$3.12 \times 10^{49}$	5.37	$8.38 \times 10^{49}$	0.015	1895	1247
Model II	C–O	$6 \times 10^9$	1.46	$3.51 \times 10^{49}$	4.32	$7.57 \times 10^{49}$	0.017	2189	1439
Model III	O–Ne–Mg	$4 \times 10^9$	1.45	$3.80 \times 10^{49}$	3.65	$6.94 \times 10^{49}$	0.018	2441	1602

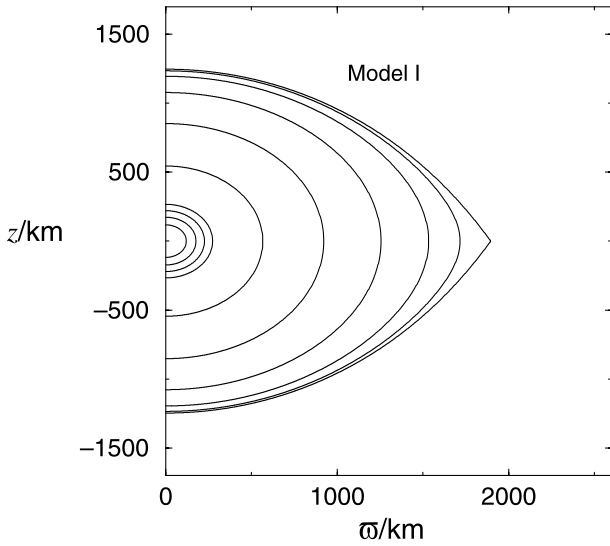


**Figure 1.** Meridional density contours of the rotating white dwarf of model I. The contours, from inward to outward, correspond to densities  $\rho/\rho_c = 0.8, 0.6, 0.4, 0.2, 0.1, 10^{-2}, 10^{-3}, 10^{-4}, 10^{-5}$  and 0.

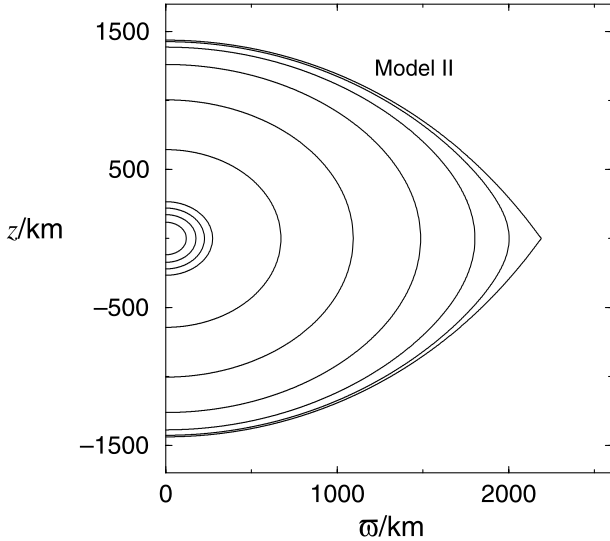


**Figure 2.** Same as Fig. 1 but for model II.

Although  $T_{\text{rot}}$  increases with  $\rho_c$ ,  $|W|$  increases at a faster rate so that  $\beta = T_{\text{rot}}/|W|$  decreases with increasing  $\rho_c$ . We also notice that the mass does not change much with increasing  $\rho_c$ . The reason is that massive white dwarfs are centrally condensed so their masses are determined primarily by the high-density central core. Here the degenerate electron gas becomes highly relativistic and the Coulomb effects are negligible, so the composition difference is irrelevant. Hence the white dwarf behaves like an  $n = 3$  polytrope, whose mass in the non-rotating case is independent of the central density.

The masses of our three models are all greater than the Chandrasekhar limit for non-rotating white dwarfs. A non-rotating C–O white dwarf with  $\rho_c = 10^{10} \text{ g cm}^{-3}$  has a radius  $R = 1300 \text{ km}$  and a mass  $M = 1.40 M_{\odot}$ . When this white dwarf is spun up to maximum rotation while keeping its mass fixed, the star puffs up to an oblate figure of equatorial radius  $R_e = 4100 \text{ km}$  and polar radius  $R_p = 2700 \text{ km}$ , and its central density drops to  $\rho_c = 5.5 \times 10^8 \text{ g cm}^{-3}$ . This peculiar behaviour is caused by the

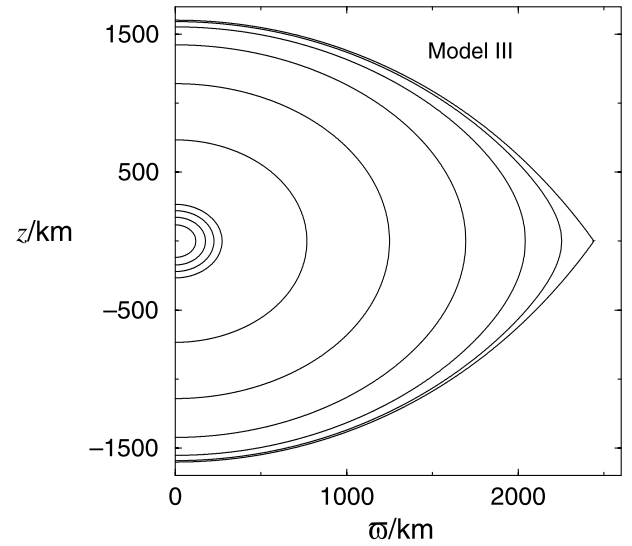


**Figure 3.** Same as Fig. 1 but for model III.

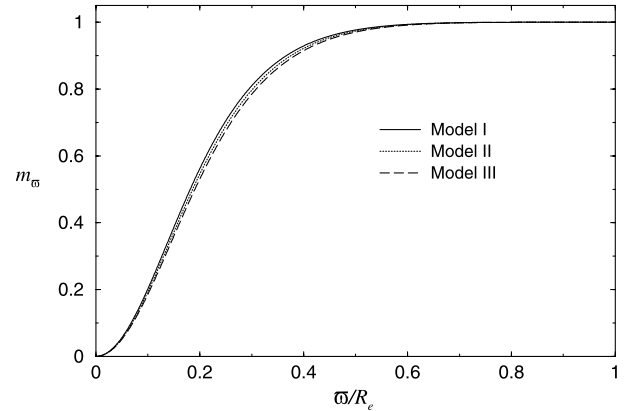


**Figure 4.** Cylindrical mass fraction  $m_{\omega}$  as a function of  $\omega$ : solid line, model I; dotted line, model II; and dashed line, model III.

soft EOS of relativistic degenerate electrons, which makes the star highly compressible and also highly expandible. When the angular velocity of the star is increased, the centrifugal force causes a large reduction in central density, resulting in a dramatic increase in the overall size of the star.

Figs 1–3 display the density contours of our three models. The contours in the high-density region remain more or less spherical even though our models represent the most rapidly rotating cases. The effect of rotation is only to flatten the density contours of the outer region in which the density is relatively low. This suggests that the white dwarfs are centrally condensed, and is clearly demonstrated in Fig. 4, where the cylindrical mass fraction

$$m_{\omega} = \frac{2\pi}{M} \int_0^{\omega} d\omega' \int_{-\infty}^{\infty} dz' \rho(\omega', z') \quad (9)$$

is plotted. In all of our three models, more than half of the mass is concentrated inside the cylinder with  $\omega \approx 0.2R_e$ .

Fig. 5 shows the specific angular momentum  $j$  as a function of the cylindrical mass fraction  $m_{\omega}$ , normalized so that  $\int_0^1 j(m_{\omega}) dm_{\omega} = 1$ . The  $j(m_{\omega})$  curves for the three models are almost indistinguishable except in the region where  $m_{\omega} \approx 1$ . The spike of the curve near  $m_{\omega} = 1$  can be understood from Fig. 4, where we see that  $m_{\omega} \approx 1$  when  $\omega/R_e \gtrsim 0.6$ . However,

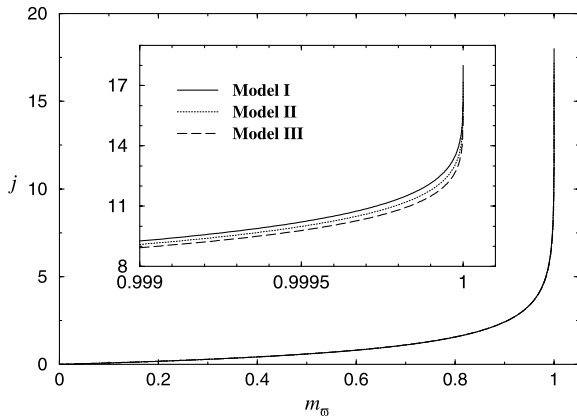


**Figure 5.** Normalized specific angular momentum  $j$  as a function of the cylindrical mass fraction  $m_\varpi$ . The curves for the three models are indistinguishable except in the region very close to  $m_\varpi = 1$ , which is magnified in the inset.

**Table 2.** The outer layers of a model I white dwarf.  $J_\varpi$  is the angular momentum of the material inside the cylinder of radius  $\varpi$ .

$\varpi/R_c$	$1 - m_\varpi$	$1 - J_\varpi/J$	$j(m_\varpi)/j(1)$
0.83	$7.5 \times 10^{-5}$	$100 \times 10^{-5}$	0.69
0.86	$3.5 \times 10^{-5}$	$49 \times 10^{-5}$	0.73
0.90	$0.65 \times 10^{-5}$	$9.8 \times 10^{-5}$	0.81
0.95	$0.027 \times 10^{-5}$	$0.45 \times 10^{-5}$	0.90

$j = (M/J)\Omega\varpi^2 \propto \varpi^2$ . These two make the values of  $j$  in the interval  $0.6^2 \lesssim j/j(m_\varpi = 1) \leq 1$  squeeze to the region  $m \approx 1$ , and the spike results. We shall point out in the next section that this spike causes a serious numerical problem in the construction of the equilibrium models of the collapsed objects. The problem can be solved by truncating the upper part of the  $j(m_\varpi)$  curve. The physical justification is that the material in the outer region contributes only a very small fraction of the total mass and angular momentum of the star, as illustrated in Table 2 for model I. The situations for the other two models are very similar and so are not shown. We see that material in the region where  $\varpi/R_c > 0.9$  [i.e.  $j(m_\varpi)/j(1) > 0.81$ ] contributes less than  $10^{-5}$  of the total mass and  $10^{-4}$  of the total angular momentum. So the upper 19 per cent of the  $j(m_\varpi)$  curve has little influence on the inner structure of the collapsed star. While this region is important for the structure of the star's outer layers, that part of the star is not of our primary interest since the mass there is too small to develop any instability that can produce a substantial amount of gravitational radiation.

### 3 COLLAPSED OBJECTS

In this section, we present the equilibrium new-born neutron-star models that may result from the collapse of the three white dwarfs computed in the previous section. Instead of performing hydrodynamic simulations, we adopt a simpler approach:

First, we assume that the collapsed stars are axisymmetric and are in rotational equilibrium with no meridional circulation. Secondly, we assume that the EOS is barotropic,  $P = P(\rho)$ . These two assumptions imply that (1) the angular velocity  $\Omega$  is a function of  $\varpi$  only, i.e.  $\partial\Omega/\partial z = 0$ , and (2) the Solberg condition is satisfied, which states that  $dj/d\varpi > 0$  for stable barotropic stars in rotational

equilibrium (see e.g. Tassoul 1978). The angular velocity profile ( $\partial\Omega/\partial z = 0$ ) is observed in the simulations of Mönchmeyer & Müller (1988) and Janka & Mönchmeyer (1989a,b). Thirdly, we are only interested in the structure of the neutron stars within a few minutes after core bounce. The time-scale is much shorter than any of the viscous time-scales, so viscosity does not have time to change the angular momentum of a fluid particle (Lindblom & Detweiler 1979; van den Horn & van Weert 1981; Goodwin & Pethick 1982; Cutler & Lindblom 1987; Sawyer 1989). Finally, we assume that no material is ejected during the collapse. It follows, from the conservation of  $j$  and the fact that  $j$  is a function of  $\varpi$  only before and after collapse, that all particles initially located on a cylindrical surface of radius  $\varpi_1$  from the rotation axis will end up being on a new cylindrical surface of radius  $\varpi_2$ . Also the Solberg condition ensures that all particles initially inside the cylinder of radius  $\varpi_1$  will collapse to the region inside the new cylinder of radius  $\varpi_2$ . Hence the specific angular momentum distribution  $j(m_\varpi)$  of the new equilibrium configuration is the same as that of the pre-collapse white dwarf; here  $m_\varpi$  is the cylindrical mass fraction defined by equation (9).

Based on these assumptions, we constructed equilibrium models of the collapsed objects with the same masses, total angular momenta and  $j(m_\varpi)$  as the pre-collapse white dwarfs.

#### 3.1 Equations of state

The gravitational collapse of a massive white dwarf is halted when the central density reaches nuclear density where the EOS becomes stiff. The core bounces back and, within a few milliseconds, a hot ( $T \gtrsim 20$  MeV), lepton-rich proto-neutron star settles into hydrodynamic equilibrium. During the so-called Kelvin–Helmholtz cooling phase, the temperature and lepton number decrease as a result of neutrino emission and the proto-neutron star cools to a cold neutron star with temperature  $T < 1$  MeV after several minutes. Since the cooling time-scale is much longer than the hydrodynamical time-scale, the proto-neutron star can be regarded as in quasi-equilibrium.

The EOS of a proto-neutron star is expressed in the form  $P = P(\rho; s, Y_e)$ , where  $s$  and  $Y_e$  are the entropy per baryon and lepton fraction respectively. As pointed out by Strobel, Schaab & Weigel (1999), the structure of a proto-neutron star can be approximated by a constant  $s$  and  $Y_e$  throughout the star, resulting in an effectively barotropic EOS.

We used two different EOS for densities above  $10^{10}$  g cm $^{-3}$ . The first is one of the standard EOS for cold neutron stars. We adopt the Bethe–Johnson EOS (Bethe & Johnson 1974) for densities above  $10^{14}$  g cm $^{-3}$ , and the BBP EOS (Baym, Bethe & Pethick 1971) for densities in the region  $10^{11}$ – $10^{14}$  g cm $^{-3}$ . It turns out that the densities of these collapsed stars are lower than  $4 \times 10^{14}$  g cm $^{-3}$ , and ideas about the EOS in this range have not changed very much since the 1970s. The second is the LPNS $_{YL04}^2$  EOS of Strobel et al. (1999).<sup>1</sup> This corresponds to a proto-neutron star 0.5–1 s after core bounce. It has an entropy per baryon  $s = 2k_B$  and a lepton fraction  $Y_e = 0.4$ , where  $k_B$  is Boltzmann's constant. We join both EOS to that of the pre-collapse white dwarf for densities below  $10^{10}$  g cm $^{-3}$ . Hereafter, we shall call the first EOS the cold EOS, and the second one the hot EOS.

<sup>1</sup>The tabulated EOS can be obtained from <http://www.physik.uni-muenchen.de/sektion/suessmann/astro/eos/>

### 3.2 Numerical method

We compute the equilibrium structure by Hachisu’s self-consistent field method modified so that  $j(m_\varpi)$  can be specified (Smith & Centrella 1992). The iteration scheme is based on the integrated static Euler equation (1) written in the form

$$h(\varpi, z) = C - \Phi(\varpi, z) + \left(\frac{J}{M}\right)^2 \int_0^\varpi d\varpi' \frac{j^2(m_{\varpi'})}{\varpi'^3}, \quad (10)$$

where  $C$  is the integration constant, and  $M$  and  $J$  are the total mass and angular momentum of the star respectively. Given an enthalpy distribution  $h_i$  everywhere, the density distribution  $\rho_i$  is calculated by the EOS and the inverse of equation (4). Next we compute the mass  $M_i$  and cylindrical mass fraction  $m_{\varpi,i}$  by

$$M_i = 4\pi \int_0^\infty d\varpi' \varpi' \int_0^\infty dz' \rho_i(\varpi', z'),$$

$$m_{\varpi,i} = \frac{4\pi}{M_i} \int_0^\varpi d\varpi' \varpi' \int_0^\infty dz' \rho_i(\varpi', z'), \quad (11)$$

and solve the Poisson equation  $\nabla^2 \Phi_i = 4\pi G \rho_i$  to obtain the gravitational potential  $\Phi_i$ . We then update the enthalpy by equation (10):

$$h_{i+1}(\varpi, z) = C_{i+1} - \Phi_i(\varpi, z) + \left(\frac{J_{i+1}}{M_{i+1}}\right)^2 \int_0^\varpi d\varpi' \frac{j^2(m_{\varpi',i})}{\varpi'^3}, \quad (12)$$

with the parameters  $C_{i+1}$  and  $(J_{i+1}/M_{i+1})^2$  determined by specifying the central density  $\rho_c$  and equatorial radius  $R_e$ . The procedure is repeated until the enthalpy and density distribution converge to the desired degree of accuracy.

To construct the equilibrium configuration with the same total mass and angular momentum as a pre-collapse white dwarf, we first compute a model of a non-rotating spherical neutron star, use its enthalpy distribution as an initial guess for the iteration scheme described above and build a configuration with slightly different  $\rho_c$  or  $R_e$ . Then the parameters  $\rho_c$  and  $R_e$  are adjusted until we end up with a configuration having the correct total mass and angular momentum.

Two numerical problems were encountered in this procedure. The first problem is that, when the angular momentum  $J$  is increased, the star becomes flattened, and the iteration often oscillates among two or more states without converging. This problem can be solved by using a revised iteration scheme suggested by Pickett et al. (1996), in which only a fraction of the revised enthalpy  $h_{i+1}$ , i.e.  $h'_{i+1} = (1 - \delta)h_{i+1} + \delta h_i$ , is used for the next iteration. Here  $\delta < 1$  is a parameter controlling the change of enthalpy. We need to use  $\delta > 0.95$  for very flattened configurations, and it takes 100–200 iterations for the enthalpy and density distributions to converge.

The second problem has to do with the spike of the  $j(m_\varpi)$  curve near  $m_\varpi = 1$  (see Fig. 5). The slope is so steep that it makes the iteration unstable. As discussed in Section 2.3, the material in the region very close to  $m_\varpi = 1$  contains a very small amount of mass and angular momentum, so we can truncate the last part of the  $j(m_\varpi)$  curve without introducing much error. Specifically, we set a parameter  $j_c < j(m_\varpi = 1)$ , and compute a quantity  $m_c$  that satisfies  $j(m_c) = j_c$ . Then we use the specific angular momentum distribution  $\tilde{j}(m_\varpi) = j(m_\varpi m_c)$  instead of  $j(m_\varpi)$ . Typically, we choose  $j_c/j(1) = 0.81$  so that  $1 - m_c \approx 10^{-5}$  (see Table 2). Hence the distributions  $\tilde{j}(m_\varpi)$  and  $j(m_\varpi)$  are basically the same except in the star’s outermost region, which is unimportant to the inner

structure of the star, and presumably also unimportant for the star’s dynamical and secular stabilities. We also tried several different values of  $j_c$  and found that the change of physical properties of the collapsed objects (e.g. the quantities in Table 3) are within the error due to our finite-size grid. Thus the truncation is also justified numerically.

We evaluate these stellar models on a cylindrical grid. This allows us to compute the integrals in equations (11) and (12) easily. We find it more convenient, however, to solve the Poisson equation for the gravitational potential on a spherical grid using the method described by Ipser & Lindblom (1990). We have verified that the potential obtained in this way agrees with the result obtained with a cylindrical multi-grid solver to within 0.5 per cent. However, the spherical grid solver (including the needed transformation from one grid to the other) is much faster than the cylindrical grid solver. The accuracy of our final equilibrium models can also be measured by the quantity  $\epsilon$  defined in equation (8). The values of  $\epsilon$  for models computed in this section are a few times  $10^{-4}$ .

### 3.3 Results

Table 3 shows some properties of the collapsed objects resulting from the collapse of the three white dwarfs in Section 2. We define the radius of gyration,  $R_g$ , and the characteristic radius,  $R_*$ , of the star by

$$MR_g^2 = \int \rho \varpi^2 d^3x \quad (13)$$

$$m_\varpi(\varpi = R_*) = 0.999. \quad (14)$$

We see that  $R_g$  and  $R_*$  that result from the same initial white dwarfs are insensitive to the neutron-star EOS, while there is a dramatic difference in the central density  $\rho_c$  and the ratio of rotational kinetic energy to gravitational potential energy  $\beta$ . The collapsed stars with the hot EOS have smaller  $\rho_c$  and  $\beta$  than those with the cold EOS. In fact, the central densities of these hot stars are less than nuclear density. It is well known that a non-rotating star cannot have a central density in the subnuclear density regime ( $4 \times 10^{11} \text{ g cm}^{-3} \lesssim \rho \lesssim 2 \times 10^{14} \text{ g cm}^{-3}$ ) because the EOS is too soft to render the star stable against gravitational collapse. It has been suggested that, if rotation is taken into account, a star with a central density in this regime can exist. Such stars are termed ‘fizzlers’ in the literature (Shapiro & Lightman 1976; Tohline 1984; Eriguchi & Müller 1985; Müller & Eriguchi 1985; Hayashi, Eriguchi & Hashimoto 1998; Imamura, Durisen & Pickett 2000).

**Table 3.** The central density  $\rho_c$ , radius of gyration  $R_g$ , characteristic radius  $R_*$  and ratio of rotational kinetic energy to gravitational energy  $\beta$  of the collapsed objects with the cold and the hot EOS.

	$\rho_c$ ( $\text{g cm}^{-3}$ )	$R_g$ (km)	$R_*$ (km)	$\beta$
Model I (cold EOS)	$3.7 \times 10^{14}$	44	67	0.230
Model I (hot EOS)	$1.4 \times 10^{14}$	46	65	0.139
Model II (cold EOS)	$3.5 \times 10^{14}$	54	80	0.246
Model II (hot EOS)	$0.79 \times 10^{14}$	59	80	0.137
Model III (cold EOS)	$3.2 \times 10^{14}$	65	94	0.261
Model III (hot EOS)	$0.27 \times 10^{14}$	73	94	0.127

However, these so-called fizzlers in our case can exist for only about 20 s before evolving to rotating cold neutron stars. In order to build a stable cold model in the subnuclear density regime, the collapsed star has to rotate much faster, which is impossible unless the pre-collapse white dwarf is highly differentially rotating.

We mention in Section 1 that Zwerger & Müller (1997) performed 2D hydrodynamic simulations of axisymmetric rotational core collapse. Their pre-collapse models are rotating stars with  $n = 3$  polytropic EOS, which is close to the real EOS of a massive white dwarf. All of their pre-collapse models have a central density of  $10^{10} \text{ g cm}^{-3}$  (see their table 1). The model A1B3 in their paper is the fastest (almost) rigidly rotating star, but its total angular momentum  $J$  and  $\beta$  are respectively 22 per cent and 40 per cent less than those of our model I of the pre-collapse white dwarf, though both have the same central density. This suggests that the structure of a massive white dwarf is sensitive to the EOS. Zwerger & Müller state in their paper that no equilibrium configuration exists that has  $\beta > 0.01$  for the (almost) rigidly rotating case. This assertion is confirmed by our numerical code. Zwerger & Müller adopt a simplified analytical EOS for the collapsing core. At the end of their simulations, the models A1B3G1–A1B3G5, corresponding to the collapsed models of A1B3, have values of  $\beta$  less than 0.07, far smaller than the  $\beta$  values of our collapsed model I (see Table 3), indicating that the EOS of the collapsed objects also play an important role in the final equilibrium configurations (or that their analysis violates one of our assumptions).

Figs 6–8 show the density contours of the collapsed objects. We see that the contours of the dense central region look like the

contours of a typical rotating star. As we go out to the low-density region, the shapes of the contours become more and more disc-like. Eventually, the contours turn into torus-like shapes for densities lower than  $10^{-4} \rho_c$ . In all cases, the objects contain two regions: a dense central core of size about 20 km and a low-density torus-like envelope extending out to 1000 km from the rotation axis. Since we truncate the  $j(m_{\varpi})$  curve, we cannot determine accurately the actual boundary of the stars. The contours shown in these figures have been checked to move less than 1 per cent as the cut-off  $j_c/j(1)$  is changed from 0.7 to 0.9. This small change is hardly visible at the displayed scales.

Fig. 9 shows the rotational frequency  $f \equiv \Omega/2\pi$  as a function of  $\varpi$ , the distance from the rotation axis. We see that the cores of the cold models are close to rigid rotation. The rotation periods of the cores of the cold neutron stars are all about 1.4 ms, slightly less than the period of the fastest observed millisecond pulsar (1.56 ms). A further analysis reveals that  $f \propto \varpi^{-\alpha}$  in the region  $\varpi \gtrsim 100$  km, where  $\alpha \approx 1.5$  for the cold models and  $\alpha \approx 1.4$  for the hot models.

To gain an insight into the structure of the envelope, we define the Kepler frequency  $\Omega_K$  at a given point on the equator as the angular frequency required for a particle to be completely supported by centrifugal force, i.e.  $\Omega_K$  satisfies the equation  $\Omega_K^2 \varpi = g$ , where  $g$  is the magnitude of gravitational acceleration at that point. Fig. 10 plots  $\Omega/\Omega_K$  as a function of  $\varpi$  along the equator. For the cold models, the curves increase from 0.5 at the centre to a maximum of about 0.95 at  $\varpi \approx 35$  km, then decrease to a local minimum of about 0.8, and then gradually increase in the outer region. The curves of the hot models, on the other hand, increase

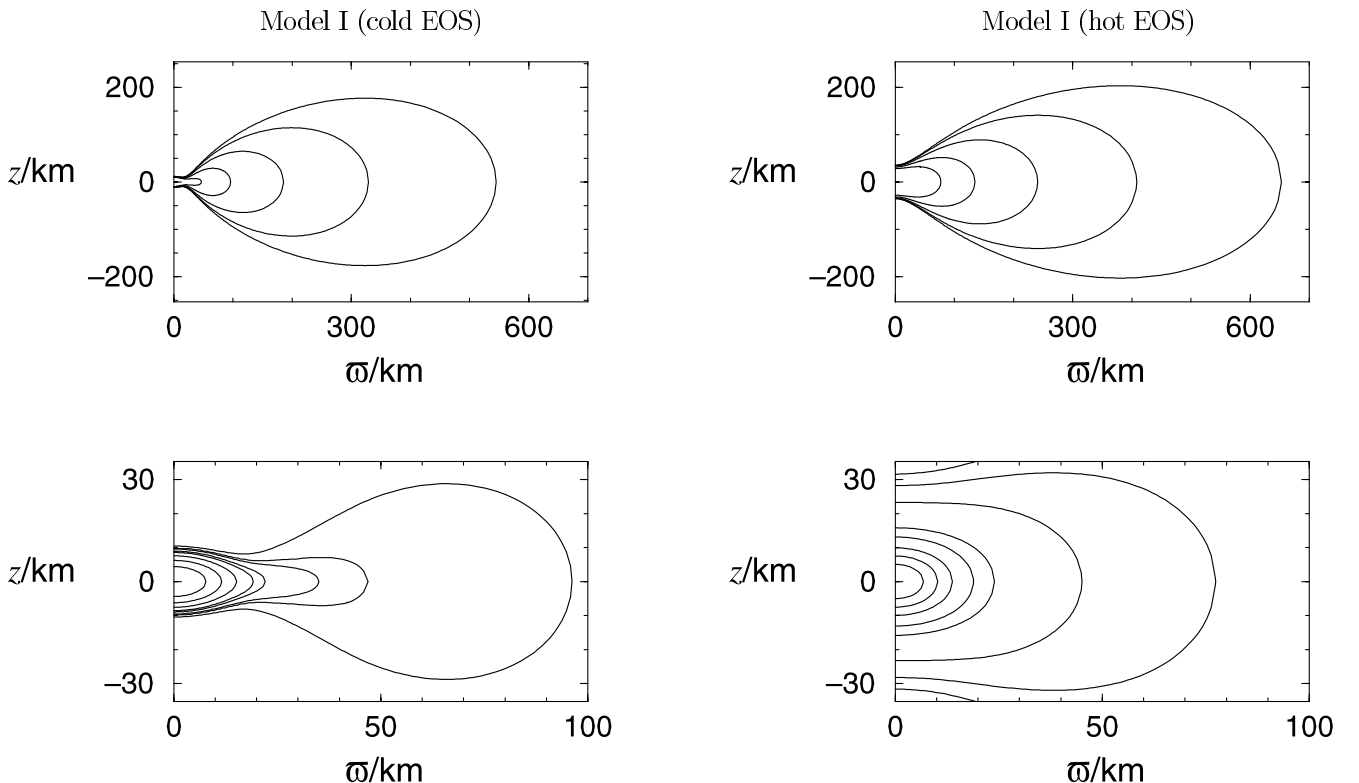


**Figure 6.** Meridional density contours of the neutron stars resulting from the collapse of a model I white dwarf. The left-hand graphs correspond to the cold EOS, and the right-hand graphs to the hot EOS. The contours in the upper graphs denote, from inward to outward,  $\rho/\rho_c = 10^{-3}, 10^{-4}, 10^{-5}, 10^{-6}$  and  $10^{-7}$ . The contours in the lower graphs denote, from inward to outward,  $\rho/\rho_c = 0.8, 0.6, 0.4, 0.2, 0.1, 10^{-2}, 10^{-3}$  and  $10^{-4}$ .

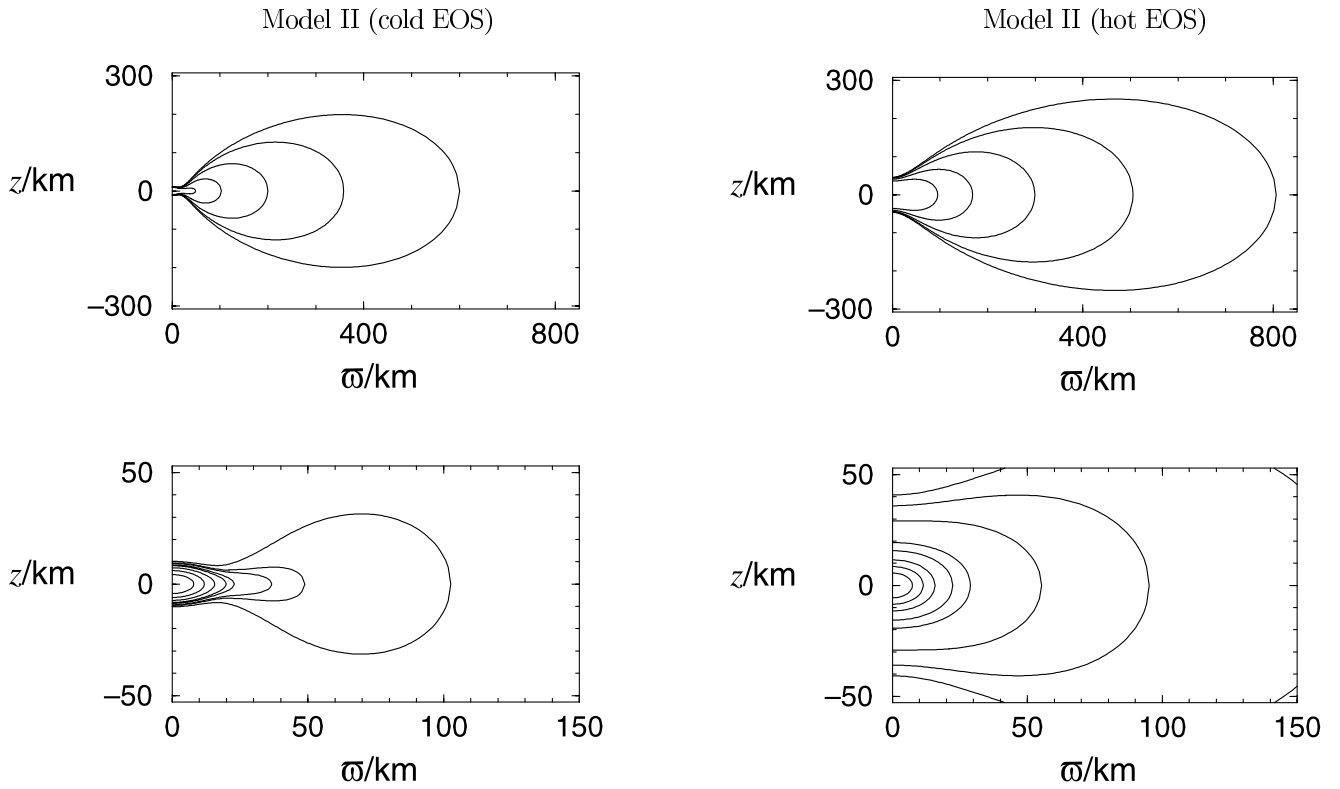


Figure 7. Same as Fig. 1 but for model II.

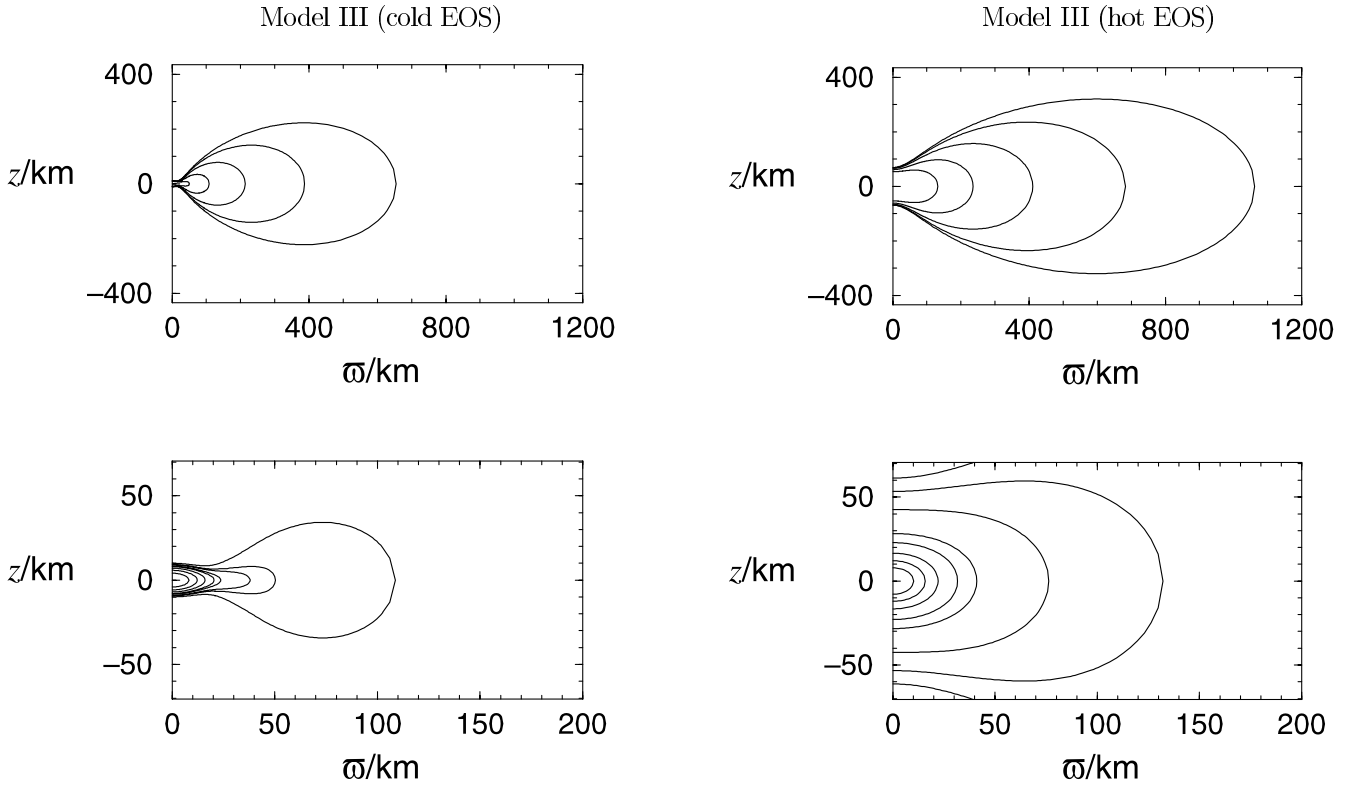


Figure 8. Same as Fig. 1 but for model III.

monotonically from about 0.4 at the centre to over 0.7 in the outer region. In all cases, centrifugal force plays an important role in the structure of the stars, especially in the low-density region.

Fig. 11 plots the cylindrical mass fraction  $m_{\varpi}$  as a function of  $\varpi$ .

In all cases the cores contain most of the mass of the stars. Material in the region  $\varpi \gtrsim 200$  km occupies only a few per cent of the total mass, but it is massive enough that its self-gravity cannot be neglected in order to compute the structure of the envelope



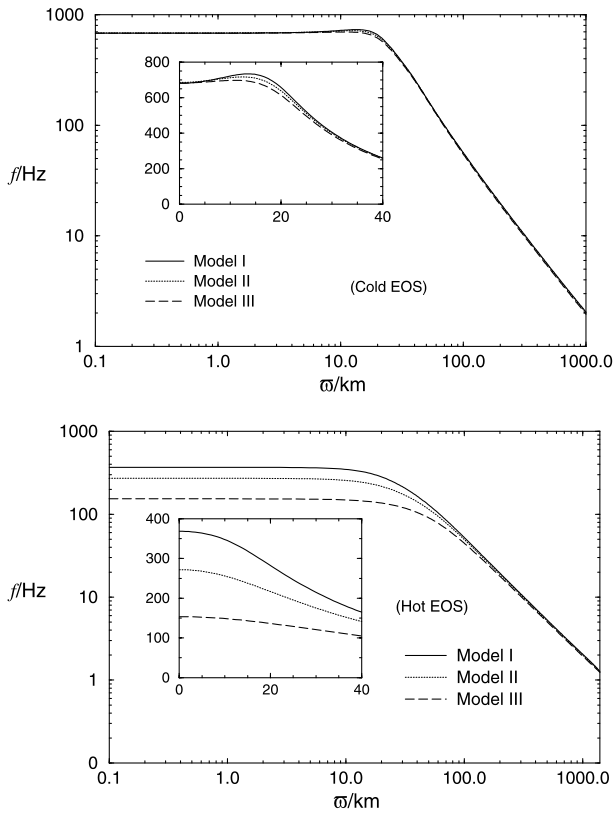


**Figure 9.** Rotational frequency  $f$  as a function of  $\omega$  for the cold models (upper graph) and the hot models (lower graph). The inset in each graph shows  $f$  in linear scale in the central region.

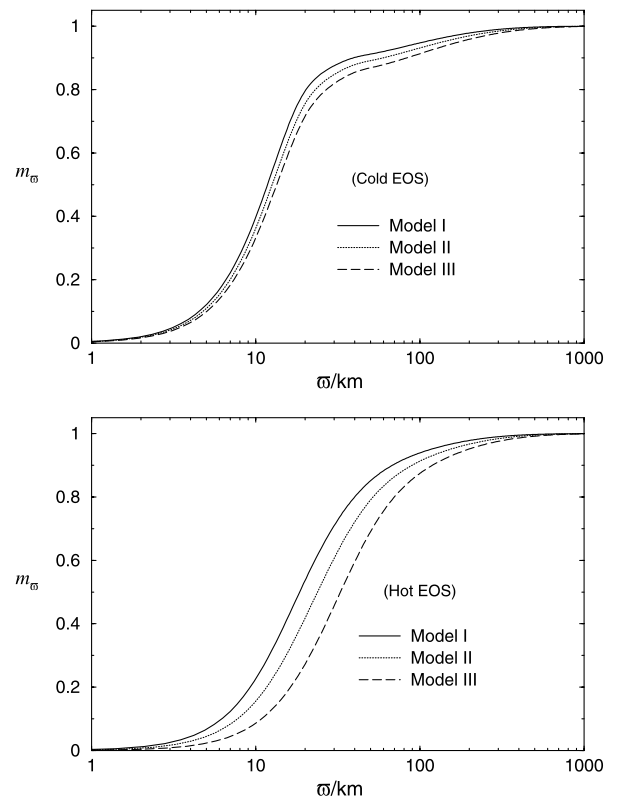


**Figure 11.** Cylindrical mass fraction  $m_\sigma$  as a function of  $\omega$  for the cold models (upper graph) and the hot models (lower graph).

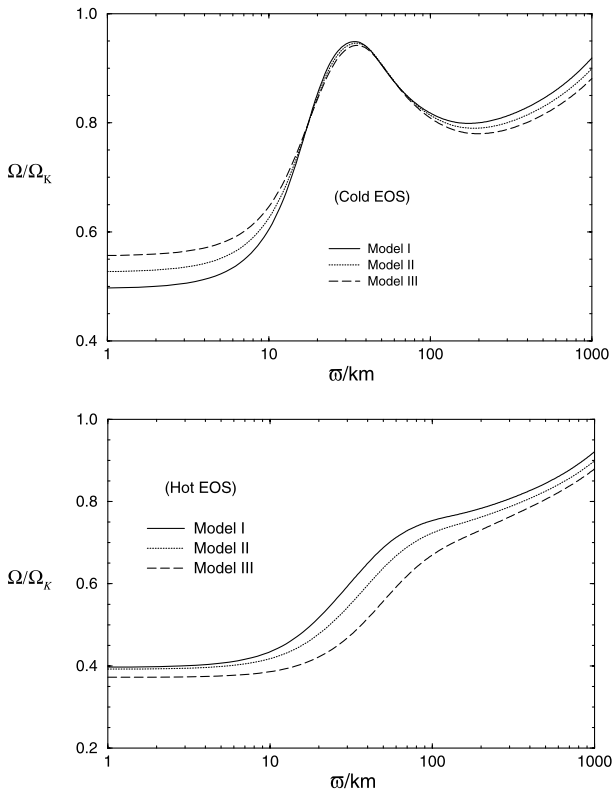


**Figure 10.** The ratio  $\Omega/\Omega_K$  along the equator as a function of  $\omega$  for the cold models (upper graph) and the hot models (lower graph).

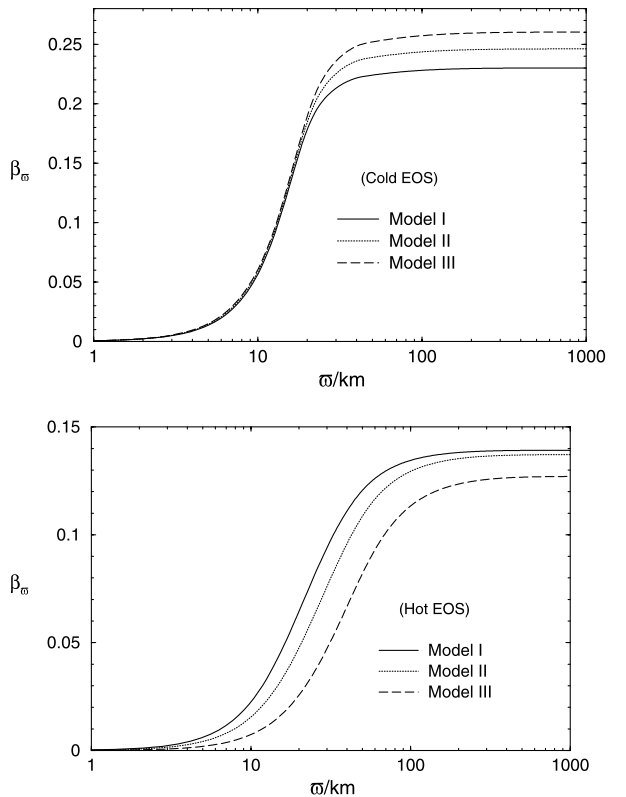


**Figure 12.** The quantity  $\beta_\sigma$  as a function of  $\omega$  for the cold models (upper graph) and the hot models (lower graph).

accurately. The envelope can be regarded as a massive, self-gravitating accretion torus. The same structure is also observed in the core collapse simulations of Janka & Mönchmeyer (1989b) and Fryer & Heger (private communication with Fryer).

Fig. 12 shows  $\beta_{\varpi} = T_{\text{rot}}(\varpi)/W(\varpi)$  as a function of  $\varpi$ , where  $T_{\text{rot}}(\varpi)$  and  $W(\varpi)$  are the rotational kinetic energy and gravitational potential energy inside the cylinder of radius  $\varpi$ , i.e.

$$T_{\text{rot}}(\varpi) = 2\pi \int_0^{\varpi} d\varpi' \varpi' (\Omega \varpi')^2 \int_0^{\infty} dz' \rho(\varpi', z') \quad (15)$$

$$W(\varpi) = 2\pi \int_0^{\varpi} d\varpi' \varpi' \int_0^{\infty} dz' \rho(\varpi', z') \Phi(\varpi', z'). \quad (16)$$

The values of  $\beta_{\varpi}$  approach  $\beta$  when  $\varpi \gtrsim 40$  km for the cold EOS models and when  $\varpi \gtrsim 100$  km for the hot EOS models. This suggests that material in the region  $\varpi \lesssim 100$  km contains a negligible amount of kinetic energy, and any instability developed in this region could not produce strong gravitational waves.

#### 4 STABILITY OF THE COLLAPSED OBJECTS

We first consider axisymmetric instabilities, i.e. axisymmetric collapse. This stability is verified when we construct the models. Recall that we start from the model of a non-rotating spherical star that is stable. Then we use it as an initial guess to build a sequence of rotating stellar models with the same specific angular momentum distribution but different total masses and angular momenta. If the final model we end up with is unstable against axisymmetric perturbations, there must be at least one model in the sequence such that

$$q \equiv \left. \frac{\partial M}{\partial \rho_c} \right|_{j(m_{\varpi}), J} = 0, \quad (17)$$

which signals the onset of instability (Bisnovatyi-Kogan & Blinnikov 1974). Here  $M$  is the total mass and  $\rho_c$  is the central density. The partial derivative is evaluated by keeping the total angular momentum  $J$  and specific angular momentum distribution  $j(m_{\varpi})$  fixed. We have verified that all of our equilibrium models in the sequences satisfy  $q > 0$ . Hence they are all stable against axisymmetric perturbations.

We next consider non-axisymmetric instabilities. We have  $\beta = 0.23$ – $0.26$  for the cold EOS models and  $\beta = 0.13$ – $0.14$  for the hot EOS models (Table 3). The hot models are probably dynamically stable but may be secularly unstable. However, since they are evolving to cold neutron stars in about 20 s and their structures are continually changing on times comparable to the secular time-scale, we shall not discuss secular instabilities of these hot models here.

The values of  $\beta$  for the three cold neutron stars are slightly less than the traditional critical value for dynamical instability,  $\beta_d \approx 0.27$ . This critical value is based on simulations of differentially rotating polytropes having the  $j(m_{\varpi})$  distribution of Maclaurin spheroids. However, recent simulations demonstrate that differentially rotating polytropes having other  $j(m_{\varpi})$  distributions can be dynamically unstable for values of  $\beta$  as low as 0.14 (Pickett et al. 1996; Centrella et al. 2000). The equilibrium configurations of some of those unstable stars also contain a low-density accretion disc-like structure in the stars' outer layers. This feature is very similar to the equilibrium structure of our models. Hence a more detailed study has to be carried out to determine whether the cold models are dynamically stable.

The subsequent evolution of a bar-unstable object has been studied for the past 15 yr (Durisen et al. 1986; Williams & Tohline 1988; Houser & Centrella 1996; Pickett et al. 1996; Smith et al. 1996; Houser 1998; New et al. 1999; Imamura et al. 2000; Brown 2000). It is found that a bar-like structure develops in a dynamical time-scale. However, it is still not certain whether the bar structure would be persistent, giving rise to a long-lived gravitational wave signal, or whether material would be shed from the ends of the bar after tens of rotation periods, leaving an axisymmetric, dynamically bar-stable central star.

Even if the cold neutron stars are dynamically stable, they are subject to various secular instabilities. The time-scale of the gravitational-wave-driven bar-mode instability can be estimated by (Friedman & Schutz 1975, 1978)

$$\tau_{\text{bar}} = 0.1 \text{ s} \left( \frac{R}{35 \text{ km}} \right)^{-5} \left( \frac{\Omega}{4000 \text{ rad s}^{-1}} \right)^{-6} \left( \frac{\beta - \beta_s}{0.1} \right)^{-5}. \quad (18)$$

In our case,  $R \approx 35$  km (see Fig. 12),  $\Omega \approx 4000 \text{ rad s}^{-1}$  and  $\beta \approx 0.24$ , so  $\tau_{\text{bar}} \sim 0.1$  s. Gravitational waves may also drive the r-mode instability (Lindblom, Owen & Morsink 1998). The time-scale is estimated by

$$\tau_r = 7.3 \text{ s} \left( \frac{\bar{\rho}}{10^{14} \text{ g cm}^{-3}} \right)^3 \left( \frac{\Omega}{4000 \text{ rad s}^{-1}} \right)^{-6} \quad (19)$$

for the  $l = 2$  r mode at low temperatures (Lindblom, Mendell & Owen 1999), where  $\bar{\rho}$  is the average density. Inserting  $\bar{\rho}$  for the inner 20-km cores of the cold stars, we have  $\tau_r \approx 10 \text{ s} \gg \tau_{\text{bar}}$ . The evolution of the bar-mode secular instability has only been studied in detail for the Maclaurin spheroids. These objects evolve through a sequence of deformed non-axisymmetric configurations eventually to settle down as a more slowly rotating stable axisymmetric star (Lindblom & Detweiler 1977; Lai & Shapiro 1995). It is generally expected that stars having more realistic EOS will behave similarly.

#### 5 CONCLUSIONS

We have constructed equilibrium models of differentially rotating neutron stars which model the end-products of the accretion-induced collapse of rapidly rotating white dwarfs. We considered three models for the pre-collapse white dwarfs. All of them are rigidly rotating at the maximum possible angular velocities. The white dwarfs are described by the EOS of degenerate electrons at zero temperature with Coulomb corrections derived by Salpeter (1961).

We assumed that (1) the collapsed objects are axisymmetric and are in rotational equilibrium with no meridional circulation, (2) the EOS is barotropic, (3) viscosity can be neglected, and (4) any ejected material carries negligible amounts of mass and angular momentum. We then built the equilibrium models of the collapsed stars based on the fact that their final configurations must have the same masses, total angular momenta and specific angular momentum distributions,  $j(m_{\varpi})$ , as the pre-collapse white dwarfs.

Two EOS have been used for the collapsed objects. One of them is one of the standard cold neutron-star EOS. The other is a hot EOS suitable for proto-neutron stars, which are characterized by their high temperature and high lepton fraction.

The equilibrium structure of the collapsed objects in all of our models consist of a high-density central core of size about 20 km, surrounded by a massive accretion torus extending over 1000 km from the rotation axis. More than 90 per cent of the stellar mass is

contained in the core and core–torus transition region, which is within about 100 km from the rotation axis (see Fig. 11). The central densities of the hot proto-neutron stars are in the subnuclear density regime ( $4 \times 10^{11} \text{ g cm}^{-3} \lesssim \rho \lesssim 2 \times 10^{14} \text{ g cm}^{-3}$ ). The structures of these proto-neutron stars are very different from those of the cold neutron stars, to which the proto-neutron stars will evolve in roughly 20 s. The proto-neutron stars have lower central densities, rotate less rapidly, and have smaller values of  $\beta$ . On the other hand, the structures of the three cold neutron stars are similar. Their central densities are around  $3.5 \times 10^{14} \text{ g cm}^{-3}$  and their central cores are nearly rigidly rotating with periods of about 1.4 ms, slightly less than the fastest observed millisecond pulsar (1.56 ms).

Zwerg & Müller (1997) performed 2D simulations of the core collapse of massive stars. The major difference between their models and ours is that they used rather simplified EOS for both the pre-collapse and the collapsed models. When compared with their fastest rigidly rotating model, A1B3, we found that their pre-collapse star has less total angular momentum and smaller  $\beta$  than the pre-collapse white dwarf of our model I, although both have the same central density. The differences between their final collapsed models (A1B3G1–A1B3G5) and ours are even more significant. The values of  $\beta$  of our collapsed objects are much larger than theirs, suggesting that the EOS plays an important role in the equilibrium configurations of both the pre-collapse white dwarfs and the resulting collapsed stars.

The values of  $\beta$  of the cold neutron stars are only slightly less than the traditional critical value of dynamical instability, 0.27, frequently quoted in the literature. The cold neutron stars may still be dynamically unstable, and a detailed study is required to settle the issue. Even if they are dynamically stable, they are still subject to various kinds of secular instabilities. A rough estimate suggests that the gravitational-wave-driven bar-mode instability dominates. The time-scale of this instability is about 0.1 s.

## ACKNOWLEDGMENTS

We thank Kip Thorne and Chris Fryer for stimulating discussions. This research was supported by NSF grants PHY-9796079, PHY-9900776 and AST-9731698, and NASA grant NAGS-4093.

## REFERENCES

- Baym G., Bethe H. A., Pethick C. J., 1971, *Nucl. Phys. A*, 175, 225  
 Bethe H. A., Johnson M. B., 1974, *Nucl. Phys. A*, 230, 1  
 Bisnovatyi-Kogan G. S., Blinnikov S. I., 1974, *A&A*, 31, 391  
 Bravo E., García-Senz D., 1999, *MNRAS*, 307, 984  
 Brown J. D., 2000, *Phys. Rev. D*, 62, 0004002  
 Burrows A., Lattimer J. M., 1986, *ApJ*, 307, 178  
 Centrella J. M., New K. C. B., Lowe L. L., Brown J. D., 2000, *ApJ*, submitted (astro-ph/0010574)  
 Chandrasekhar S., 1969, *Ellipsoidal Figures of Equilibrium*. Yale Univ. Press, New Haven, CT  
 Cutler C., Lindblom L., 1987, *ApJ*, 314, 234  
 Durisen R. H., Gingold R. A., Tohline J. E., Boss A. P., 1986, *ApJ*, 305, 281  
 Eriguchi Y., Müller E., 1985, *A&A*, 147, 161  
 Finn L. S., Evans C. R., 1990, *ApJ*, 351, 588  
 Friedman J. L., Schutz B. F., 1975, *ApJ*, 199, L157  
 Friedman J. L., Schutz B. F., 1978, *ApJ*, 221, L99  
 Goodwin B. T., Pethick C. J., 1982, *ApJ*, 253, 816  
 Hachisu I., 1986, *ApJS*, 61, 479  
 Hayashi A., Eriguchi Y., Hashimoto M., 1998, *ApJ*, 492, 286  
 Houser J. L., 1998, *MNRAS*, 209, 1069  
 Houser J. L., Centrella J. M., 1996, *Phys. Rev. D*, 54, 7278  
 Houser J. L., Centrella J. M., Smith S., 1994, *Phys. Rev. Lett.*, 72, 1314  
 Imamura J. N., Toman J., 1995, *ApJ*, 444, 363  
 Imamura J. N., Durisen R. H., Pickett B. K., 2000, *ApJ*, 528, 946  
 Ipser J. R., Lindblom L., 1990, *ApJ*, 355, 226  
 Janka H.-Th., Mönchmeyer R., 1989a, *A&A*, 209, L5  
 Janka H.-Th., Mönchmeyer R., 1989b, *A&A*, 226, 69  
 Lai D., Shapiro W. L., 1995, *ApJ*, 442, 259  
 Lindblom L., Detweiler S. L., 1977, *ApJ*, 211, 565  
 Lindblom L., Detweiler S. L., 1979, *ApJ*, 232, L101  
 Lindblom L., Owen B. J., Morsink S. M., 1998, *Phys. Rev. Lett.*, 80, 4843  
 Lindblom L., Mendell G., Owen B. J., 1999, *Phys. Rev. D*, 60, 064006  
 Mönchmeyer R., Müller E., 1988, in Ögelman H., ed., *NATO ASI on Timing Neutron Stars*. Reidel, Dordrecht  
 Mönchmeyer R., Schäfer G., Müller E., Katea R. E., 1991, *A&A*, 246, 417  
 Müller E., Eriguchi Y., 1985, *A&A*, 152, 325  
 Müller E., Hillebrandt W., 1981, *A&A*, 103, 358  
 New K. C. B., Centrella J. M., Tohline J. E., 1999, *Phys. Rev. D*, 62, 064006  
 Nomoto K., 1982, *ApJ*, 253, 798  
 Nomoto K., 1987, in Ulmer M., ed., *Proc. 13th Texas Symp. on Relativistic Astrophysics*. World Scientific, Singapore  
 Nomoto K., Kondo Y., 1991, *ApJ*, 367, L19  
 Ogata S., Iyetomi H., Ichimaru S., 1991, *ApJ*, 372, 259  
 Pickett B. K., Durisen R. H., Davis G. A., 1996, *ApJ*, 458, 714  
 Rapp M., Müller E., Ruffert M., 1998, *A&A*, 332, 969  
 Saijo M., Shibata M., Baumgarte T. W., Shapiro S. L., 2000, *ApJ*, 548, 919  
 Salpeter E. E., 1961, *ApJ*, 134, 669  
 Salpeter E. E., Van Horn H. M., 1969, *ApJ*, 155, 183  
 Sawyer R. F., 1989, *Phys. Rev. D*, 39, 3804  
 Shapiro S. L., Lightman A. P., 1976, *ApJ*, 207, 263  
 Shibata M., Baumgarte T. W., Shapiro S. L., 2000, *ApJ*, 542, 453  
 Smith S., Centrella J. M., 1992, in d’Inverno R., ed., *Approaches to Numerical Relativity*. Cambridge Univ. Press, New York  
 Smith S., Houser J., Centrella J. M., 1996, *ApJ*, 458, 236  
 Stergioulas N., Friedman J. L., 1998, *ApJ*, 492, 301  
 Strobel K., Schaab C., Weigel M. K., 1999, *A&A*, 350, 497  
 Tassoul J.-L., 1978, *Theory of Rotating Stars*. Princeton Univ. Press, Princeton, NJ  
 Thorne K. S., 1995, in Sasaki M., ed., *Proc. 8th Nishinomiya–Yukawa Memorial Symp. on Relativistic Cosmology*. Universal Academy Press, Tokyo  
 Timmes F. S., Woosley S. E., 1992, *ApJ*, 396, 649  
 Tohline J. E., 1984, *ApJ*, 285, 721  
 Tohline J. E., Durisen R. H., McCollough M., 1985, *ApJ*, 298, 220  
 van den Horn L. J., van Weert Ch. G., 1981, *ApJ*, 251, L97  
 Williams H. A., Tohline J. E., 1988, *ApJ*, 334, 449  
 Zwerg T., Müller E., 1997, *A&A*, 320, 209

This paper has been typeset from a  $\text{\TeX}/\text{\LaTeX}$  file prepared by the author.